Optoelectronic manifestation of orbital angular momentum driven by chiral hopping in helical Se chains

Bumseop Kim[1,6], Dongbin Shin[2,3,6], Seon Namgung[1], Noejung Park[1], Kyoung-Whan Kim[4*], Jeongwoo Kim[5*]

[1]*Department of Physics, Ulsan National Institute of Science and Technology, Ulsan 44919, Korea*

[2]*Department of Physics and Photon Science, Gwangju Institute of Science and Technology, Gwangju 61005, Korea*

[3]*Max Planck Institute for the Structure and Dynamics of Matter and Center for Free Electron Laser Science, 22761 Hamburg, Germany*

[4]*Center for Spintronics, Korea Institute of Science and Technology, Seoul 02792, Korea*

[5]*Department of Physics, Incheon National University, Incheon 22012, Korea*

[6]These authors contributed equally: Bumseop Kim, Dongbin Shin

*corresponding author e-mail

kwk@kist.re.kr; kjwlou@inu.ac.kr

Abstract

Chiral materials have garnered significant attention in the field of condensed matter physics. Nevertheless, the magnetic moment induced by the chiral spatial motion of electrons in helical materials, such as elemental Te and Se, remains inadequately understood. In this work, we investigate the development of quantum angular momentum enforced by chirality using static and time-dependent density functional theory calculations for an elemental Se chain. Our findings reveal the emergence of an unconventional orbital texture driven by the chiral geometry, giving rise to a non-vanishing current-induced orbital moment. By incorporating spin-orbit coupling, we demonstrate that a current-induced spin accumulation arises in the chiral chain, which fundamentally differs from the conventional Edelstein effect. Furthermore, we demonstrate the optoelectronic detection of the orbital angular momentum in the chiral Se chain, providing a conceptually novel alternative to the interband Berry curvature, which is ill-defined in low dimensions.

Introduction

The concept of chirality has emerged as an essential factor in condensed matter physics, playing a crucial role in determining nontrivial band topology and exotic spin texture[1-4]. The intimate relation between momentum and spin, which is enforced by chirality, has been studied in a variety of systems, including the chiral anomaly of Weyl semimetals[5-8], high-fold chiral fermions[2,9-12], chiral domain walls[13], and magnetic skyrmions[14]. Moreover, the chiral spatial motion dictated by helical geometry is closely related to the dynamics of spin angular momentum (SAM) as demonstrated by the chirality-induced spin selectivity[3,15-17] and the chiral magnetic effect[18]. Intriguingly, the observed spin magnetic moment induced by the chiral motion in helical materials is significantly greater, by one to three orders of magnitude, than that predicted by the classical solenoid model[19]. This large discrepancy indicates the existence of a strong quantum-mechanical interplay between the motion of electron and its SAM in chiral systems.

Elemental Te and Se represent a promising platform for exploring the intricacies of the interwoven orbital motion and magnetism due to its helical atomic structure and strong spin-orbit coupling (SOC)[20,21]. The trigonal-stacked crystal structure of Te and Se consists of one-dimensional chains with three-fold screw rotation symmetry[22,23], thereby enabling facile control over size and thickness in low dimensions[24-26]. In Te nanowires, a large chirality-dependent magnetoresistance is observed along the helical chain, and its induced magnetism is several orders of magnitude larger than in non-chiral systems[27-29]. The sizable magnetic moment is expected to be the result of the Edelstein effect, which refers to the spin accumulation induced by a flowing charge current[30,31]. As evidenced by the Rashba-Edelstein effect, spin-momentum locking is required for the current-induced spin accumulation[32]. In the case of Te chains, the radial spin texture in momentum space (see Fig. 1b for example), a unique

spin-momentum locking of chiral chains, is a key ingredient responsible for the large current-induced magnetism[21,33,34].

Nevertheless, as implied by the discrepancy of the spin magnetic moment between theory and experiment in chiral materials, the fundamental physics underlying the distinctive spin-momentum locking and the microscopic mechanism governing the large current-induced magnetism in the chiral chain systems have not been sufficiently investigated. Although previous helical model studies presented a close correlation between the radial spin texture and the inherent geometry of helical chains[19,23,35-37], the quantum mechanical origin underpinning this association remains elusive. Given that orbital angular momentum (OAM) can also be created by an external electric field in helical chains, it is imperative to clarify its contribution to the induced magnetic moment and its interaction with SAM through strong SOC.

In this study, we examined the spontaneous development of coupled OAM and SAM induced by the helical geometry in chiral Se chains. We also investigated the quantum mechanical behaviour of excited carriers in non-equilibrium states under the influence of diverse external fields using real-time time-dependent density functional theory (TDDFT). It is found that the chiral hopping between the p-orbitals of an individual Se chain produces a notable orbital polarisation in the vicinity of the Fermi level. This chiral OAM gives rise to a distinct spin polarisation via strong SOC, which corresponds to the radial spin texture observed in bulk. Our simulation demonstrates that the current-induced magnetism in chiral chains is primarily driven by quantum superposition of the orbital states, which is clearly distinct from the conventional Edelstein effect that arises from the slight shift of the Fermi surface. We also present a novel method for detecting the intriguing OAM embedded in the chiral Se chain using the one-to-one correspondence between OAM and photocurrent. We unveil how the spin and orbital degrees of freedom are entangled in a helical chain, the quantum mechanical counterpart

of a classical solenoid, and provide a powerful but convenient method to realise the hidden chirality-induced OAM.
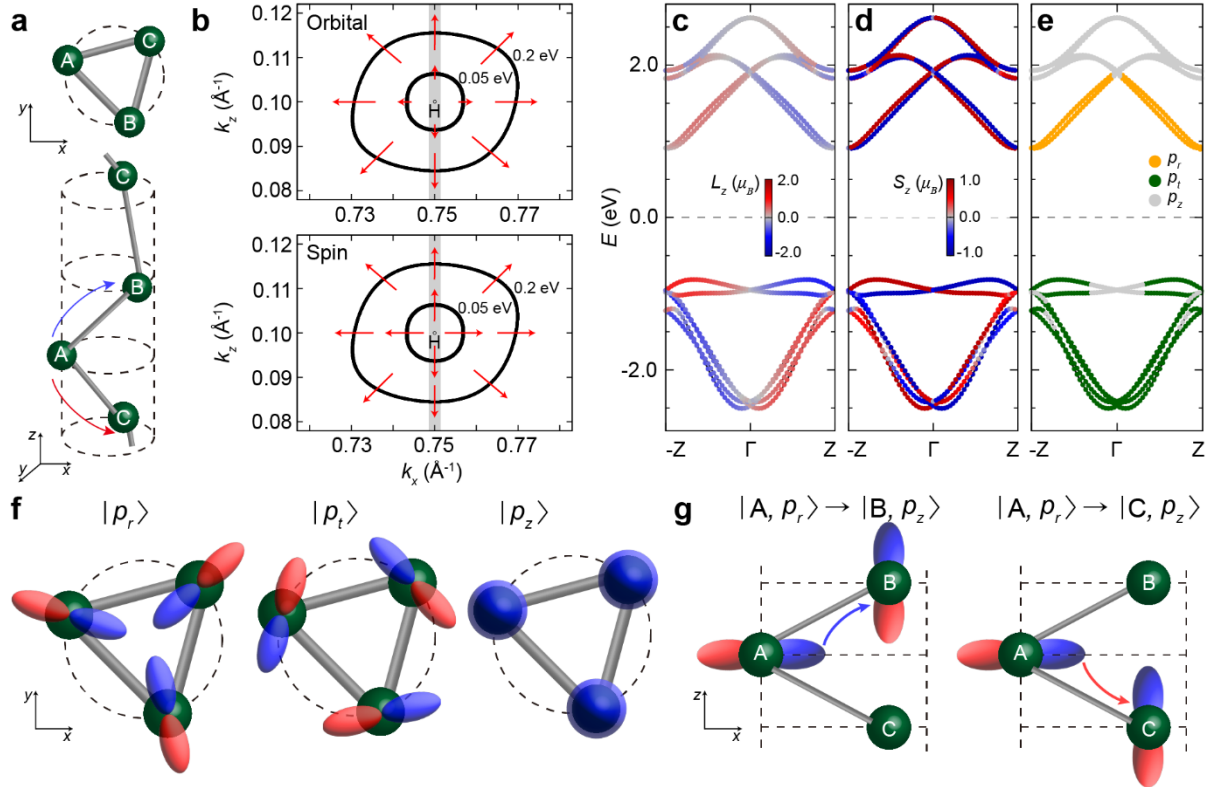
Fig. 1 | Orbital/Spin angular momentum of a helical Se chain. a Top and side views of a single chain of elemental Se with three different atomic sites (A, B, and C). **b** Orbital and spin angular momentum profiles of the conduction band minimum at the H point in bulk Se. Black contour lines denote energy levels of 0.05 and 0.2 eV, respectively, and gray lines represent the one-dimensional Brillouin zone of an individual Se chain. **c-e** Calculated band structure of the Se chain with (**c**) orbital-angular-momentum resolution (L_z), (**d**) spin-angular-momentum resolution (S_z), and (**e**) atomic-orbital resolution using radial (p_r), tangential (p_t), and axial (p_z) p-orbitals as the orbital bases. **f** Schematic drawing of the p_r, p_t, and p_z orbitals. **g** Graphical illustration of asymmetric orbital hopping between p_r and p_z in a single Se chain.

Results

Orbital and spin angular momentum texture in a chiral Se chain

We elucidate the correlation between the helical geometry of a chiral Se chain and its unique OAM and SAM texture through electronic structure calculations. The Se chain exhibits

threefold screw-axis symmetry, as depicted in Fig. 1a, and stack to form a trigonal elemental Se crystal, as shown in Supplementary Fig. 1. Bulk Se has a radial orbital and spin texture resembling hedgehogs near the Fermi level at the H point[21,27], as illustrated in Fig. 1b, indicating the orbital-momentum and spin-momentum locking. Interestingly, this radial OAM is preserved even without the inclusion of SOC, as shown in Supplementary Fig. 2, while the characteristic spin structure is disrupted.

We investigate whether the distinct OAM and SAM texture of the chiral Se arises from its helical geometry of the single chain or from the staking of multiple chains. To this end, we compare the orbital and spin structure of the axial line of bulk Se (gray lines of Fig. 1b) with those of the single chiral chain (Fig. 1c-e). The radial angular momentum of the stack of the chains successfully corresponds to the orbital/spin polarisation parallel to the chain direction (k_z) in the one-dimensional Brillouin zone, implying that the intriguing electronic structure is primarily influenced by the intrachain effect of the single Se chain. The absence of mirror symmetry allows for the non-vanishing out-of-plane orbital/spin component in the Se chain, and time-reversal symmetry enforces the zero net moment, consequently satisfying the relations such that $\langle \hat{L}_z \rangle_{n,k_z} = -\langle \hat{L}_z \rangle_{n,-k_z}$, and $\langle \hat{S}_z \rangle_{n,k_z} = -\langle \hat{S}_z \rangle_{n,-k_z}$. The polarised states near the Fermi level primarily originate from p-orbitals. To account for the helical nature of the chain, we adopt a cylindrical p-orbital basis. Specifically, while the valence bands consist mainly of the tangential (p_t) and axial (p_z) orbitals, the conduction bands are derived from the radial (p_r) orbitals (Fig. 1e, f). As in the bulk, the one-dimensional orbital texture persists even in the absence of SOC as demonstrated in Supplementary Fig. 3.

To understand the underlying physics behind the unconventional OAM and SAM texture originating from the unique geometry of the chiral Se chain, we develop an analytic model Hamiltonian based on the tight-binding approximation[38-41]. By considering the nearest

hoppings between three *p*-orbital states for each of the three atoms in the Se chain (Fig. 1a), we obtain a 9 × 9 Hamiltonian matrix as follows,

$$H = \begin{pmatrix} h_{\text{on}} & h_{\text{hop}} & h_{\text{hop}}^{\dagger} \\ h_{\text{hop}}^{\dagger} & h_{\text{on}} & h_{\text{hop}} \\ h_{\text{hop}} & h_{\text{hop}}^{\dagger} & h_{\text{on}} \end{pmatrix},$$ (1)

where the on-site Hamiltonian h_{on} and the hopping Hamiltonian h_{hop} are 3 × 3 matrices in the *p*-orbital space. The on-site Hamiltonian is modeled as $h_{\text{on}} = \epsilon_r |p_r\rangle\langle p_r| + \epsilon_t |p_t\rangle\langle p_t| + \epsilon_z |p_z\rangle\langle p_z|$, where ϵ_α denotes the on-site energy for the p_α orbital. The use of the cylindrical basis (Fig. 1f) allows us to express the off-diagonal part in terms of a single matrix h_{hop}, referred to as the 'hopping-down' Hamiltonian, which describes the nearest hopping in the direction of C → B → A → C. In contrast, the hopping in the opposite direction is given by $h_{\text{hop}}^{\dagger}$, the 'hopping-up' Hamiltonian. By carefully examining the signs of the hopping integrals for all hopping procedures (see Fig. 1g for examples), we model h_{hop} as

$$h_{\text{hop}} = e^{ik_z a} \begin{pmatrix} t_{rr} & -t_{tr} & -t_{zr} \\ t_{tr} & t_{tt} & t_{zt} \\ t_{zr} & t_{zt} & t_{zz} \end{pmatrix},$$ (2)

in the (p_r, p_t, p_z) basis. Here $t_{\beta\alpha}$ denotes the hopping integral for $\alpha \to \beta$ hopping and *a* represents the one-third of the length of the unit cell, which corresponds to the distance between the nearest sites along the *z*-axis, giving rise to the Bloch-like factor $e^{ik_z a}$. The anti-symmetric nature of t_{tr} and t_{zr} for the hopping-up and hopping-down, as exemplified in Fig. 1g, is rooted in the unique geometry of the helical Se chain and turns out to be a crucial factor in the emergence of the OAM texture shown in Fig. 1c. We demonstrate this below through equations (3)-(4).

To reproduce the OAM texture with reduced reliance on SOC (Supplementary Figs. 2, 3), we focus on the orbital degree of freedom by diagonalizing the Hamiltonian [equation (1)]

while disregarding the spin degree of freedom. The hopping integrals are treated perturbatively to avoid the technical complexity of exact diagonalisation, resulting in the nine eigenstates $|\widetilde{p_\alpha,\mu}\rangle$ presented in Supplementary Note 1. In this notation, $\alpha = r, t, z$ refers to the orbital states, $\mu = -1, 0, 1$ denotes the atomic degree of freedom. The tilde on the states indicates that they are perturbed by electron hopping, and they are expressed as a superposition of the unperturbed states $|p_\beta, \mu\rangle$. In Supplementary Note 2, we explicate the consistency between the eigenstates from the model Hamiltonian and the band structure from our first-principles calculations (Fig. 1c-e). One can calculate the OAM expectation values from the eigenstates using $L_z = (i\hbar/2)(|p_t\rangle\langle p_r| - |p_r\rangle\langle p_t|)$ and obtain

$$\langle\widetilde{p_z,\mu}|L_z|\widetilde{p_z,\mu}\rangle = \frac{4\hbar t_{zr}t_{zt}\cos\left(k_z a + \frac{2\pi\mu}{3}\right)\sin\left(k_z a + \frac{2\pi\mu}{3}\right)}{(\epsilon_z - \epsilon_r)(\epsilon_z - \epsilon_t)}, \tag{3}$$

$$\langle\widetilde{p_t,\mu}|L_z|\widetilde{p_t,\mu}\rangle = -\langle\widetilde{p_r,\mu}|L_z|\widetilde{p_r,\mu}\rangle = \frac{2\hbar t_{tr}\sin\left(k_z a + \frac{2\pi\mu}{3}\right)}{\epsilon_t - \epsilon_r}. \tag{4}$$

This simplified model effectively captures the essential characteristics of the numerical results, such as the band splitting and the sign change of OAM at the zone center, as exhibited in Supplementary Fig. 3. The anti-symmetric hopping enables the quantum mechanical superpositions of atomic orbitals that are energetically separated, leading to the non-vanishing orbital distribution in momentum space. In this aspect, our approach is distinct from previous models dealing with a helical geometry without incorporating the orbital degree of freedom[30,31] which derive a non-zero OAM distribution from inter-atomic hoppings. In Supplementary Fig. 4, we demonstrate that the inter-atomic contribution is negligible near the Fermi level in the Se chain, and thus the consideration of the orbital degree of freedom is essential to describe the intriguing orbital structure of the helical chain.

We incorporate the spin degree of freedom into our model Hamiltonian to investigate

how spin and orbital degrees of freedom are intertwined by the presence of SOC in the Se chain.

In the absence of SOC, the SAM lacks any directional preference and consequently a particular spin texture does not occur. In the presence of SOC ($\eta_{SO}\mathbf{L}\cdot\mathbf{S}$), the spin degeneracy is lifted in accordance with the relative orientation of SAM and OAM [equations (3) and (4)], thereby creating a spin polarisation $\langle S_z\rangle = (\nu\hbar/2)\,\mathrm{sgn}(\langle L_z\rangle)$ that is either parallel or antiparallel to the OAM, where $\nu = \pm 1$ is the spin quantum number. Therefore, we can conclude that the OAM is a more fundamental degree of freedom that gives rise to the SAM texture in the Se chain[42]. In this regard, our model offers a concrete instance of a recent theoretical proposition[43], which posits the essential significance of the orbital degree of freedom in the long-range spin transport in DNA-like materials[3,44-46].
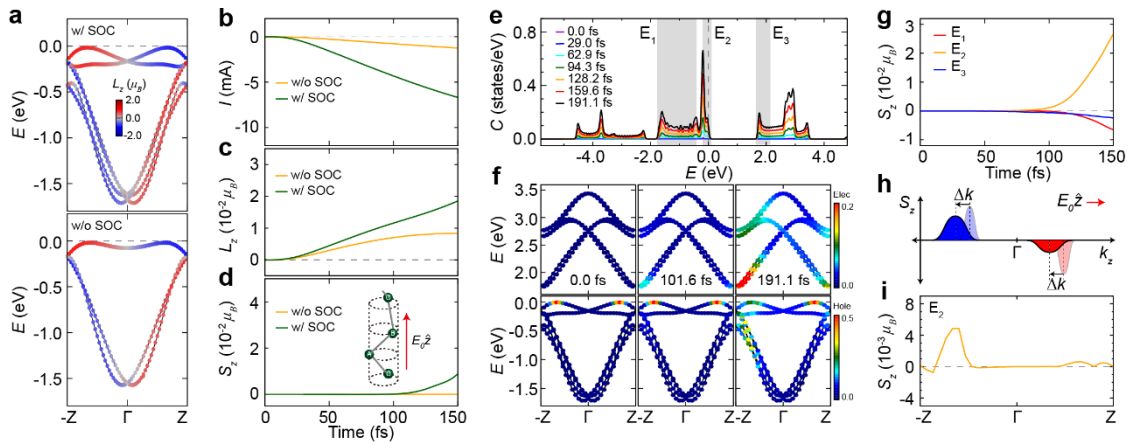
Fig. 2 | Current-induced magnetism in a helical Se chain. a Calculated band structure of a Se chain with orbital-angular-momentum resolution (L_z) under hole doping (0.1 e/unit) in the presence or absence of SOC. **b-d** Calculated (**b**) induced current (I), (**c**) total orbital angular momentum (L_z), and (**d**) total spin angular momentum (S_z) induced by a dc field (10^{-3} V/Å) along the Se chain, as illustrated in the inset of (**d**). The quantitative definitions of I, L_z, and S_z are described in the Methods section. **e** Time evolution of the density of states projected onto the unperturbed electron/hole states in the Se chain. **f** Time evolution of the electron/hole weights projected onto the ground-state band structure of the Se chain. **g** Time evolution of the decomposed spin angular momentum of the Se chain for three energy ranges (E_1, E_2, and E_3) as shown in the gray regions of (**e**). **h** Schematic illustration of the conventional Edelstein effect, in which a net spin magnetic moment is generated by the Fermi surface shift triggered by an external field. **i** Calculated momentum-resolved spin angular momentum for the major E_2 contribution in the Se chain at 191.1 fs. The spin distribution of the chiral chain is distinguished from that of the conventional Edelstein effect shown in (**h**).

Nonequilibrium generation of orbital and spin magnetism

Drawing on a fundamental understanding of the interplay between the OAM and the SAM in the Se chain, we investigate the time-dependent dynamics of these quantities in non-equilibrium under the influence of an external field. By utilizing TDDFT calculations, we reproduce the excited states in a single Se chain and identify the emergent magnetism and its dominant mechanism. To simulate metallic nanowires used in the experiment, we employed a hole-doped (0.1 e/unit) Se chain, in which the Fermi level touches the valence bands, as shown in Fig. 2a, while preserving its original OAM distribution. We also considered an external dc field (10^{-3} V/Å) to mimic the current-induced magnetism observed in the experiment[27]. A detailed description of the methodology used to estimate the time-evolving electric current, OAM, and SAM is provided in the Methods section. Unlike the immediate response of electric current and orbital magnetism, which begin to arise at 10 fs and increase monotonically (Fig. 2b, c), the development of non-zero spin magnetism in the Se chain requires a substantial time delay (100 fs) and is dependent on SOC, as depicted in Fig. 2d. This suggests that the orbital magnetism drives the spin part through SOC. Furthermore, the dominance of orbital magnetism at the early stage under an external field is also observed in a helical Te chain (Supplementary Fig. 5).

We conduct an in-depth analysis to understand the formation of finite orbital and spin magnetism in the Se chain by tracking the real-time nonequilibrium states projected onto the ground states. The density of states of the excited states extends over a wide range from -4 to 4 eV (Fig. 2e), and we found that the overall shape is independent of the external field strength (Supplementary Fig. 6). Such a widespread excitation originates from the strong mixing of the orthogonal orbitals via the helical structure of the Se chain. As shown in Fig. 1a, f, the shapes of the tangential orbital of the A site and the radial orbital of the B site are similar to each other,

leading to considerable overlap of the orbitals under the external field along the z direction. As a result, the strong mixing gives a widespread distribution in Fig. 2e when projected to the unperturbed eigenstates.

The widespread density of state is observed not only in energy, but also in momentum space as shown in Fig. 2f. The projection of the excited states onto the ground electronic structure exhibits an asymmetric k-distribution of nonequilibrium weights within the lowest conduction band near the zone boundary at 101.6 fs, while maintaining a symmetric distribution in the highest valence band. This finding indicates that the induced orbital magnetisation of the early time (< 100 fs) is facilitated by the imbalanced transition to the conduction bands with different orbital polarisation (Fig. 1c). However, the equal weights of the conduction bands with different spin polarisation inhibit the occurrence of a spin magnetisation (Fig. 1d). Thus, the emergent total OAM remains unaffected by the absence of SOC, as demonstrated in Supplementary Fig. 7. At 191.1 fs, the excited state displays the imbalanced momentum distribution within the valence bands, which coincides with the onset of the spin magnetisation (Fig. 2f, g). The formation of spin magnetism in the chiral Se chain is primarily attributed to the partial occupancy of the highest spin-split valence bands in the E_2 region, as shown in Fig. 2g. It is important to note that this mechanism differs from the conventional Edelstein effect, in which a shift of the Fermi surface induced by an electrostatic field give rise to a net spin polarisation due to opposite spin-momentum locking at $+k$ and $-k$ points[47], as illustrated in Fig. 2h. In the Se chiral chain, however, the net magnetisation does not originate from the spin difference between $+k$ and $-k$ points, but between the highest valence bands with opposite spin polarisations at the same point as shown in Fig. 2i.

Our findings signify a quantum-mechanical development of orbital magnetisation under an axial electric field by the imbalanced distribution of excited states, giving rise to an

accompanied spin magnetisation induced by the unique interconnection of orbital and spin triggered by the helical geometry. It should be noted that this study does not take into account various scattering sources, such as phonons and defects. Therefore, to avoid misinterpretation, we focus solely on the early stages of the time dynamics of the excited state.
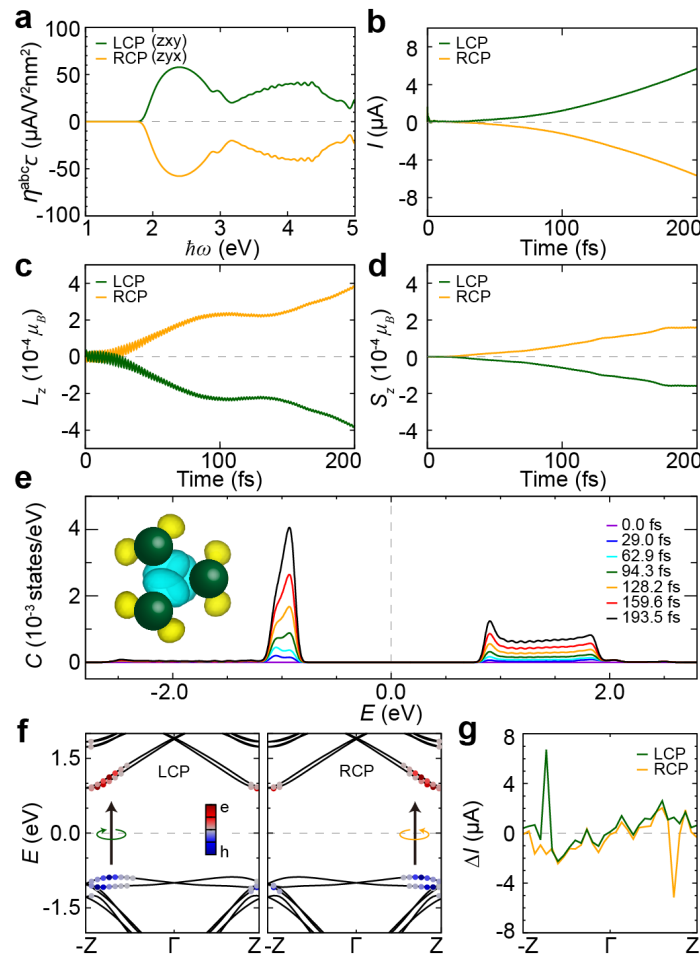
Fig. 3 | Circular photogalvanic effect in a helical Se chain. a Calculated circular photogalvanic current (injection current) spectrum of a Se chain as a function of the frequency of a left or right circularly polarised light (LCP or RCP). **b-d** Calculated (**b**) induced current (I), (**c**) total orbital angular momentum (L_z), and (**d**) total spin angular momentum (S_z) induced by circularly polarised lights with intensity of 0.051 V/Å and frequency of $\hbar\omega$=2.02 eV as a function of time. **e** Time evolution of the electron/hole-carrier density of states in the Se chain under a circularly polarised light. The inset represents a real-space representation of the generated electron/hole carriers. Yellow and cyan iso-surfaces denotes the excited hole and electron density, respectively. **f** Electron/hole carrier occupancies projected onto the ground-state band structure of the Se chain under LCP or RCP at t=193.4 fs. **g** Momentum-resolved photogalvanic current density under LCP or RCP in the Se chain at t=193.4 fs.

Optoelectronic detection of orbital angular momentum

In order to appreciate the physical significance of the OAM generated in the chiral structure, we shall proceed to examine a comprehensive operator expression of the OAM. The lateral confinement of electron motion to a finite region in a one-dimensional system enables an expression of the L_z operator in terms of position operators : $L_z = (m_e/2i\hbar)(\{x, [y, H]\} - \{y, [x, H]\})$, where m_e is the electron mass and H is the Hamiltonian. The OAM expectation value for an eigenstate $|n\rangle$ of H is then $\langle n|L_z|n\rangle = (2m_e/\hbar)\text{Im}\sum_{n'}(\epsilon_n - \epsilon_{n'})\langle n|x|n'\rangle\langle n'|y|n\rangle$, where ϵ_n is the energy eigenvalue of $|n\rangle$. Provided that the dominant contribution of the OAM comes from the pair of the highest valence band (v) and the lowest conduction band (c), the OAM is simply given by

$$\langle c|L_z|c\rangle \approx \langle v|L_z|v\rangle \approx \frac{2m_e}{\hbar}\text{Im}[(\epsilon_c - \epsilon_v)\langle c|x|v\rangle\langle v|y|c\rangle]. \tag{5}$$

The right-hand side is referred as to the two-band OAM, denoted as $\langle L_z\rangle_{cv}$. In Supplementary Fig. 8, we offer numerical validation of the two-band approximation in our system by demonstrating the resemblance between the total OAM and the two-band OAM. The significance of the two-band OAM in the reduced dimension lies in its feasibility to be measured by the circular photogalvanic effect (CPGE) beyond mere theoretical speculation. By modifying the well-established CPGE formalism[48] with our two-band OAM, we obtain the circular photogalvanic current J (i.e., injection current) in the low-dimension. Specifically, the injection current is given by

$$J = -\frac{2\pi\tau}{m_e\hbar^2\omega}e^3E^2\langle L_z\rangle_{cv}, \tag{6}$$

where ω and E is the frequency and the electric field of the incident light, respectively, and τ is the relaxation time. The derivation of equation (6) is explicated in Supplementary Note 3. In two or three dimensions with periodic boundary conditions, the CPGE is explained in terms of

two-band Berry curvature[48]. However, in a one-dimensional system, the Berry curvature is ill-defined and requires a generalisation through the adoption of position operators[49]. Conversely, the OAM is inherently defined in a confined space, making it a more suitable physical quantity to quantify the optical response of a low-dimensional system.

To explicitly demonstrate the intimate relationship between the OAM and the CPGE, we utilise second-order perturbation theory to evaluate the response function of the injection current. As predicted in equation (6), the injection current is created under a circularly polarised light with above-band-gap frequency in the helical Se chain (Fig. 3a). The injection current can be switched by the chirality of the chain as well as the helicity of light (Supplementary Fig. 9), indicating the generated photocurrent serves as a reference for determining the chain's chirality.

We also confirm the photocurrent generation in the Se chain by applying a circularly polarised light ($\hbar\omega$=2.02 eV) through TDDFT calculations as presented in Fig. 3b. As a secondary effect owing to the selective excitation of orbital/spin-polarised electrons, the generated current carries induced orbital and spin magnetism in the chain (Fig. 3c, d), which can be controlled by the helicity of applied light even in a very strong field limit (Supplementary Fig. 10). The monotonic increasing number of electron and hole carriers near the Fermi level with time (Fig. 3e) clearly implies that the CPGE of the Se chain is governed by the band edge transition corresponding to the frequency of the applied light. As expected from Fig. 1e, the hole (electron) carriers are predominantly composed of the p_t (p_r) orbitals in the CPGE of the Se chain (the inset of Fig. 3e). The projection of the excited state onto the ground band structure exhibits uneven excitation caused by circularly polarised light (Fig. 3f)[50,51], leading to a non-zero photocurrent that strongly localises near the zone boundary and depends on the helicity of external light (Fig. 3g). Hence, the intriguing OAM texture

embedded in the chiral structure can be readily realised by detecting the generated photocurrent in response to circularly polarised light.
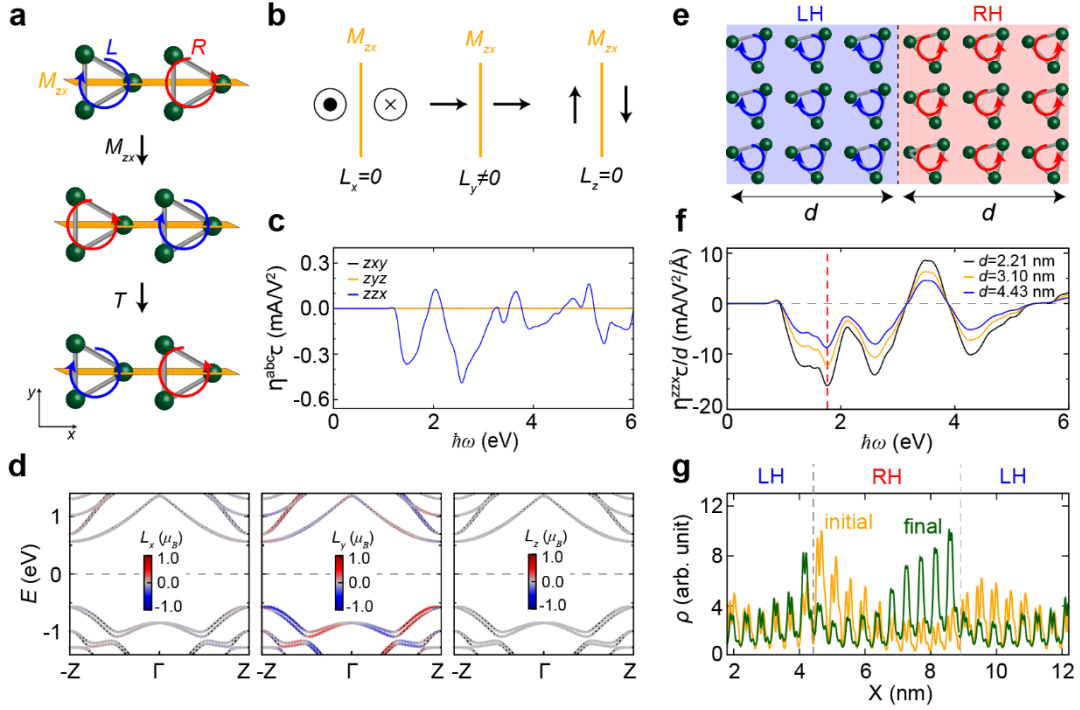
Fig. 4 | Detection of boundary states using the circular photogalvanic effect. a Schematic drawing of hypothetical two-dimensional helical Se layers consating of alternating left-handed (*L*) and right-handed (*R*) configurations. The alternating chains are invariant under consecutive *zx* mirror (M_{zx}) and translation (*T*) operations. **b** M_{zx} mirror operation on each component of the orbital angular momentum in the alternating chains, which enforces the vanishing *x*-and *z*-components of orbital angular momentum along the one-dimensional chain direction. **c** Calculated circular photogalvanic current (injection current) spectrum of the alternating chains as a function of the frequency of applied circularly polarised lights. The *zx*-plane polarisation (blue) induces a non-zero photocurrent, while *xy*-plane (black) or *yz*-plane (yellow) polarisation result in a zero current. **d** Calculated band structure of the alternating chains with orbital-angular-momentum resolution. **e** Schematic drawing of a boundary between left-handed (LH) and right-handed (RH) chains. **f** Variation in the injection current spectrum per unit length of the domain structure upon the domain length (*d*). **g** The average charge density profiles of the initial and final states of an excitation triggered by an external light with $\hbar\omega$ = 1.76 eV, corresponding to the red dotted line in (**f**).

We extend the concept of optoelectronic detection of the concealed orbital polarisation to a more intricate and realistic system, wherein extrinsic OAM that is otherwise prohibited in bulk is enforced by spatial symmetry. As a simplified case study to elucidate the relationship

between the presence of photocurrent and OAM determined by geometric symmetry, we consider a two-dimensional Se structure with alternating chirality along the x direction as illustrated in Fig. 4a. Our hypothetical structure possesses a combined symmetry of zx-plane mirror (M_{zx}) and translation (T), which nullifies the x and z components of OAM as shown in Fig. 4b (see Supplementary Note 4 for a more comprehensive elucidation). One can easily generalise the photogalvanic current of equation (6) for different light proportion directions, and the survival of the L_y component can be interpreted as the activation of photocurrent under circularly polarised light with a zx rotating plane. In line with our symmetry analysis, the alternating two-dimensional system allow for the presence of the y component of OAM (Fig. 4d), which is absent in a single Se chain (Supplementary Fig. 11), leading to a non-zero photocurrent in a wide energy range under zx-circularly polarised light (Fig. 4c).

The essential physics underlying the artificial alternating chains can be applied to a more pragmatic system featuring opposite chiralities, namely the domain boundary between left-handed (LH) and right-handed (RH) domains as presented in Fig. 4e. The circular photogalvanic current along the chain under the zx-circular polarisation, normalised by the domain size (d), decreases as the domain size increases (Fig. 4f), implying its interface-localised nature resulting from the switching of the chirality. We check that excited carriers generated by an external light with $\hbar\omega = 1.76$ eV (red vertical line in Fig. 4f) are distributed across the domain boundary by computing the charge density distribution of the initial and final states. Importantly, this interface photocurrent is not observed in the bulk without a boundary (Supplementary Fig. 12). The strong correlation between OAM and photocurrent is further evidenced by the non-negligible L_y value observed across the entire k_z line (Supplementary Fig. 13). Such a photocurrent is also produced at the edge between Se chains and vacuum as shown in Supplementary Fig. 14, signaling the viability and applicability of OAM engineering and its optoelectronic detection.

Discussion

In summary, we revealed the quantum mechanical origin of the chirality-driven OAM and its manifestation by means of electrical/optical drives in a helical Se chain. Our model for the helical chain showed the anti-symmetric chiral hopping produces a unique orbital texture parallel to its momentum, generating a radial spin profile with the aid of strong SOC. The intermixing of orthogonal p orbital states and asymmetric nonequilibrium distribution gives rise to a net orbital magnetism under an external electric field, accompanied by a net spin magnetism due to the partial occupancy of spin-split states in the presence of SOC. This induced magnetism is quantum mechanically distinguished from the conventional Edelstein effect in Rashba SOC systems. We also demonstrated the generation of photocurrent can be expressed in terms of OAM in low dimensions, which provides an alternative to the poorly defined Berry curvature in a non-periodic system. The close connection between OAM and photocurrent enables the optoelectronic manifestation of the intriguing orbital polarisation inherent in the chiral chain. Furthermore, we showed that, by tuning the geometric symmetry at an interface or edge, a previously forbidden component of OAM can be allowed, leading to the generation of edge-localised photocurrent. Our results provide a fundamental understanding of the interplay between spin and orbital degrees of freedom in chiral geometries, which paves the way for design of novel orbitronic/spintronic devices utilizing chiral materials.

Methods

Electronic structure calculation. We carried out density functional theory (DFT) calculations using the projector-augmented plane-wave method[52], as implemented in the Vienna Ab initio Simulation Package (VASP)[53]. The Perdew–Burke–Ernzerhof (PBE) functional of the generalised gradient approximation was employed to describe the exchange–correlation interactions among electrons[54]. The bulk Se chains were optimised with the van der Waals interaction until the maximum forces were less than 0.001 eV Å^{-1}, and the vacuum layer was set to be greater than 10 Å to simulate the one-dimensional Se chain. The energy cutoff for the plane-wave-basis expansion was set at 400 eV. We used a 10×10×8 k-point grid for the bulk Se chains and a 1×1×15 k-point grid for the one-dimensional Se chain.

Circular photogalvanic response using perturbation theory. The injection-current spectra were evaluated from the tight-binding Hamiltonian based on maximally localised Wannier functions[55] using the second-order optical response formalism[56].

$$\eta^{abc}(\omega) = \frac{e^3\pi}{2\hbar^2} \int \frac{d\mathbf{k}}{8\pi^3} \sum_{nm} \Delta^a_{mn} f_{nm} (r^c_{mn} r^b_{nm} - r^b_{mn} r^c_{nm}) \delta(\omega_{mn} - \omega)$$

where a, b, c are Cartesian indices and $r^a_{nm} = i\langle n|\partial_{k_a}|m\rangle$ is interband Berry connection. f_{nm} is occupation difference between band n and m, and $\hbar\Delta^a_{mn} = v^a_{mm} - v^a_{nn}$ is the group velocity difference between band n and m. For the injection-current estimation, a 3×3×100 k-point grid was adopted for calculating the one-dimensional Se chains. This is a sufficiently dense mesh of grids to show convergence of the injection-current spectra.

Real-time calculation of the electric current, OAM, and SAM. To examine the electric current, OAM, and SAM, we performed real-time TDDFT calculations using the plane-wave-based real-time evolution[57,58]. In our calculations, the Kohn–Sham wavefunction, the density, and the Hamiltonian were self-consistently evolved through the time-dependent equation:

$$i\hbar\frac{\partial}{\partial t}\psi_{n,\mathbf{k}}(\mathbf{r},t) = \left[\frac{1}{2m_e}\left(\frac{\hbar}{i}\nabla + \frac{e}{c}\mathbf{A}_{\text{ext}}(t)\right)^2 + \sum_{\lambda} v_{\text{atom}}(\mathbf{R}_{\lambda}(t)) + V_{\text{DFT}}[\rho(\mathbf{r},t)]\right]\psi_{n,\mathbf{k}}(\mathbf{r},t)$$

where n and $\mathbf{k}$ denote the band index and the Bloch momentum vector, respectively. $\mathbf{A}_{\text{ext}}$ and V_{DFT} indicate the time-dependent vector potential and DFT potential, respectively. The discretised time step for the time integration (Δt) was set to 2.415 as. In our calculations, the electric field was expressed using the velocity gauge of the vector potential via the relation $\mathbf{E}(t) = -\frac{1}{c}\partial\mathbf{A}_{\text{ext}}/\partial t$. We considered two different electric fields in our calculation: DC-field $\mathbf{E}_{\text{DC}}(t) = E_{\text{DC}}\hat{z}$ and AC-field $\mathbf{E}_{\text{AC}}(t) = E_{\text{AC}}\sin(\omega t)\hat{z}$. The initial wavefunctions $[\psi_{n,\mathbf{k}}(t = 0)]$ were obtained from the static-ground-state DFT calculations using the QUANTUM ESPRESSO package with the PBE exchange–correlation functional. Using the time-evolving Bloch wavefunctions, we evaluated the time profile of the electric current, OAM, and SAM as follows[59,60]:

$$I(t) = -\frac{e}{m_e}\sum_{n}\sum_{\mathbf{k}} f_{n,\mathbf{k}}\langle\psi_{n,\mathbf{k}}(t)|\hat{\boldsymbol{\pi}}|\psi_{n,\mathbf{k}}(t)\rangle$$

$$L_z(t) = \sum_{n}\sum_{\mathbf{k}} f_{n,\mathbf{k}}\langle\psi_{n,\mathbf{k}}(t)|\hat{x}\hat{\pi}_y - \hat{y}\hat{\pi}_x|\psi_{n,\mathbf{k}}(t)\rangle$$

$$S_z(t) = \sum_{n}\sum_{\mathbf{k}} f_{n,\mathbf{k}}\langle\psi_{n,\mathbf{k}}(t)|\hat{S}_z|\psi_{n,\mathbf{k}}(t)\rangle$$

where n is the band index, $f_{n,\mathbf{k}}$ is the initial occupation of the Bloch state, m_e is the mass of an electron. The gauge-invariant mechanical momentum is defined as $\widehat{\boldsymbol{\pi}} = \frac{m_e}{i\hbar}\left[\widehat{\mathbf{r}}, \widehat{H}\right] = \widehat{\mathbf{p}} + \frac{e}{c}\mathbf{A}_{\text{ext}}(t) + i\frac{m_e}{\hbar}[V_{\text{NL}}, \widehat{\mathbf{r}}]$. Here $\hat{x}, \hat{y}$ are the position operator along the x- and y-axis, respectively, and $\hat{S}_z$ is the SAM operator along the z-axis.

Data availability

The authors declare that the main data supporting the findings of this study are available within the article and its Supplementary information files.

Code availability

The tight-binding code for computing the injection current spectra is partially available from the github: https://github.com/BSKim12/Shift_current.git.

References

1   Chang, G. *et al.* Topological quantum properties of chiral crystals. *Nat. Mater.* **17**, 978-985 (2018).

2   Rao, Z. *et al.* Observation of unconventional chiral fermions with long Fermi arcs in CoSi. *Nature* **567**, 496-499 (2019).

3   Göhler, B. et al. Spin selectivity in electron transmission through self-assembled monolayers of double-stranded DNA. *Science* **331**, 894–897 (2011)

4   Yang, S.-H., Naaman, R., Paltiel, Y. & Parkin, S. S. P. Chiral spintronics. *Nat. Rev. Phys.* **3**, 328-343 (2021).

5   Rees, D. et al. Helicity-dependent photocurrents in the chiral Weyl semimetal RhSi. *Sci. Adv*. **6**, eaba0509 (2020).

6   Chang, G. *et al.* Unconventional Photocurrents from Surface Fermi Arcs in Topological Chiral Semimetals. *Phys. Rev. Lett.* **124**, 166404 (2020).

7   Ma, J. *et al.* Unveiling Weyl-related optical responses in semiconducting tellurium by mid-infrared circular photogalvanic effect. *Nat. Commun.* **13**, 5425 (2022).

8   Zhao, Y. F. *et al.* Creation of chiral interface channels for quantized transport in magnetic topological insulator multilayer heterostructures. *Nat. Commun.* **14**, 770 (2023).

9   Sanchez, D. S. *et al.* Topological chiral crystals with helicoid-arc quantum states. *Nature* **567**, 500-505 (2019).

10   Sanchez, D. S. *et al.* Tunable topologically driven Fermi arc van Hove singularities. *Nat. Phys.* (2023).

11   Takane, D. *et al.* Observation of Chiral Fermions with a Large Topological Charge and Associated Fermi-Arc Surface States in CoSi. *Phys. Rev. Lett.* **122**, 076402 (2019).

12   Schröter, N. B. M. *et al.* Chiral topological semimetal with multifold band crossings and long Fermi arcs. *Nat. Phys.* **15**, 759-765 (2019).

13   Yang, S.-H., Garg, C. & Parkin, S. S. P. Chiral exchange drag and chirality oscillations in synthetic antiferromagnets. *Nat. Phys.* **15**, 543-548 (2019).

14   Nagaosa, N. & Tokura, Y. Topological properties and dynamics of magnetic skyrmions. *Nat. Nanotechnol.* **8**, 899-911 (2013).

15   Ray, K., Ananthavel, S., Waldeck, D. & Naaman, R. Asymmetric scattering of polarized electrons by organized organic films of chiral molecules. *Science* **283**, 814–816 (1999).

16   Liu, Y., Xiao, J., Koo, J. & Yan, B. Chirality-driven topological electronic structure of DNA-like materials. *Nat. Mater.* **20**, 638-644 (2021).

17   Naaman, R. & Waldeck, D. H. Chiral-Induced Spin Selectivity Effect. *J. Phys. Chem. Lett.* **3**, 2178-2187 (2012).

18   Li, Q. *et al.* Chiral magnetic effect in ZrTe5. *Nat. Phys.* **12**, 550-554 (2016).

19   Gersten, J., Kaasbjerg, K. & Nitzan, A. Induced spin filtering in electron transmission through chiral molecular layers adsorbed on metals with strong spin-orbit coupling. *J. Chem. Phys.* **139**, 114111 (2013).

20   Starkloff, T. & Joannopoulos, J. D. The electronic structure of trigonal Se and Te for pressure near the phase transition points. *J. Chem. Phys.* **68**, 579-584 (1978).

21   Hirayama, M., Okugawa, R., Ishibashi, S., Murakami, S. & Miyake, T. Weyl Node and Spin Texture in Trigonal Tellurium and Selenium. *Phys. Rev. Lett.* **114**, 206401 (2015).

22   Nakayama, K. *et al.* Band splitting and Weyl nodes in trigonal tellurium studied by angle-resolved photoemission spectroscopy and density functional theory. *Phys. Rev. B* **95**, 125204 (2017).

23   Maruggi, G. P., Ferreira, J., Baggio-Saitovitch, E., Enderlein, C. & Silva Neto, M. B. Hedgehog orbital texture in p-type tellurium and the antisymmetric nonreciprocal Hall response. *Phys. Rev. Mater.* **7**, 014204 (2023).

24   Wang, Y. *et al.* Field-effect transistors made from solution-grown two-dimensional tellurene. *Nat. Electron.* **1**, 228-236 (2018).

25   Niu, C. *et al.* Gate-tunable strong spin-orbit interaction in two-dimensional tellurium probed by weak antilocalization. *Phys. Rev. B* **101**, 205414 (2020).

26   Qiu, G. *et al.* Quantum Hall effect of Weyl fermions in n-type semiconducting tellurene. *Nat. Nanotechnol.* **15**, 585-591 (2020).

27   Calavalle, F. *et al.* Gate-tuneable and chirality-dependent charge-to-spin conversion in tellurium nanowires. *Nat. Mater.* **21**, 526-532 (2022).

28   Furukawa, T., Shimokawa, Y., Kobayashi, K. & Itou, T. Observation of current-induced bulk magnetization in elemental tellurium. *Nat. Commun.* **8**, 954 (2017).

29   Furukawa, T., Watanabe, Y., Ogasawara, N., Kobayashi, K. & Itou, T. Current-induced magnetization caused by crystal chirality in nonmagnetic elemental tellurium. *Phys. Rev. Res.* **3**, 023111 (2021).

30   Yoda, T., Yokoyama, T. & Murakami, S. Orbital Edelstein Effect as a Condensed-Matter Analog of Solenoids. *Nano. Lett.* **18**, 916-920 (2018).

31   Yoda, T., Yokoyama, T. & Murakami, S. Current-induced Orbital and Spin Magnetizations in Crystals with Helical Structure. *Sci. Rep.* **5**, 12024 (2015).

32   Roy, A. *et al.* Long-range current-induced spin accumulation in chiral crystals. *npj Comput. Mater.* **8**, 243 (2022).

33   Sakano, M. *et al.* Radial Spin Texture in Elemental Tellurium with Chiral Crystal Structure. *Phys. Rev. Lett.* **124**, 136404 (2020).

34   Gatti, G. *et al.* Radial Spin Texture of the Weyl Fermions in Chiral Tellurium. *Phys. Rev. Lett.* **125**, 216402 (2020).

35   Varela, S., Medina, E., Lopez, F. & Mujica, V. Inelastic electron scattering from a helical potential: transverse polarization and the structure factor in the single scattering approximation. *J. Phys. Condens. Matter.* **26**, 015008 (2014).

36   Yeganeh, S., Ratner, M. A., Medina, E. & Mujica, V. Chiral electron transport: scattering through helical potentials. *J. Chem. Phys.* **131**, 014707 (2009).

37   Eremko, A. A. & Loktev, V. M. Spin sensitive electron transmission through helical potentials. *Phys. Rev. B* **88**, 165409 (2013).

38   Varela, S., Mujica, V. & Medina, E. Effective spin-orbit couplings in an analytical tight-binding model of DNA: Spin filtering and chiral spin transport. *Phys. Rev. B* **93**, 155436 (2016).

39   Varela, S. *et al.* Intrinsic Rashba coupling due to hydrogen bonding in DNA. *J. Chem.*

Phys. **151**, 125102 (2019).

40   Geyer, M., Gutierrez, R., Mujica, V. & Cuniberti, G. Chirality-Induced Spin Selectivity in a Coarse-Grained Tight-Binding Model for Helicene. *J. Phys. Chem. C* **123**, 27230-27241 (2019).

41   Torres, J. D., Hidalgo-Sacoto, R., Varela, S. & Medina, E. Mechanically modulated spin-orbit couplings in oligopeptides. *Phys. Rev. B* **102**, 035426 (2020).

42   Otsuto, R., Yatabe, Y. & Akera, H. Orbital and spin polarizations induced by current through a helical atomic chain. *Phys. Rev. B* **104**, 035431 (2021).

43   Han, S., Lee, H. W. & Kim, K. W. Orbital Dynamics in Centrosymmetric Systems. *Phys. Rev. Lett.* **128**, 176601 (2022).

44   Xie, Z. *et al.* Spin specific electron conduction through DNA oligomers. *Nano. Lett.* **11**, 4652-4655 (2011).

45   Suda, M. *et al.* Light-driven molecular switch for reconfigurable spin filters. *Nat. Commun.* **10**, 2455 (2019).

46   Shiota, K. *et al.* Chirality-Induced Spin Polarization over Macroscopic Distances in Chiral Disilicide Crystals. *Phys. Rev. Lett.* **127**, 126602 (2021).

47   Kovacs-Krausz, Z. *et al.* Electrically Controlled Spin Injection from Giant Rashba Spin-Orbit Conductor BiTeBr. *Nano. Lett.* **20**, 4782-4791 (2020).

48   Xu, S.-Y. *et al.* Electrically switchable Berry curvature dipole in the monolayer topological insulator WTe2. *Nat. Phys.* **14**, 900-906 (2018).

49   Kim, K.-W., Jeong, H., Kim, J. & Jin, H. Vertical transverse transport induced by hidden in-plane Berry curvature in two dimensions. *Phys. Rev. B* **104**, L081114 (2021).

50   Kim, J. *et al.* Prediction of ferroelectricity-driven Berry curvature enabling charge- and spin-controllable photocurrent in tin telluride monolayers. *Nat. Commun.* **10**, 3965 (2019).

51   Jnawali, G. *et al.* Ultrafast photoinduced band splitting and carrier dynamics in chiral tellurium nanosheets. *Nat. Commun.* **11**, 3991 (2020).

52   Kresse, G. & Joubert, D. From ultrasoft pseudopotentials to the projector augmented-wave method. *Phys. Rev. B* **59**, 1758 (1999).

53   Kresse, G. & Hafner, J. Ab initio molecular dynamics for liquid metals. *Phys. Rev. B* **47**, 558-561 (1993).

54   Perdew, J. P., Burke, K. & Ernzerhof, M. Generalized Gradient Approximation Made Simple. *Phys. Rev. Lett.* **77**, 3865 (1996).

55   Mostofi, A. A. *et al.* wannier90: A tool for obtaining maximally-localised Wannier functions. *Comput. Phys. Commun.* **178**, 685-699 (2008).

56   Sipe, J. E.& Shkrebtii, A. I. Second-order optical response in semiconductors. *Phys. Rev. B* **61**, 5337 (2000).

57   Giannozzi, P. *et al.* QUANTUM ESPRESSO: a modular and open-source software project for quantum simulations of materials. *J. Phys. Condens. Matter.* **21**, 395502 (2009).

58   Shin, D., Lee, G., Miyamoto, Y. & Park, N. Real-Time Propagation via Time-Dependent Density Functional Theory Plus the Hubbard U Potential for Electron-Atom Coupled Dynamics Involving Charge Transfer. *J. Chem. Theory Comput.* **12**, 201-208

(2016).

59   Shin, D. *et al.* Unraveling materials Berry curvature and Chern numbers from real-time evolution of Bloch states. *Proc. Natl. Acad. Sci. U.S.A.* **116**, 4135-4140 (2019).

60   Kim, B., Park, N. & Kim, J. Giant bulk photovoltaic effect driven by the wall-to-wall charge shift in WS2 nanotubes. *Nat. Commun.* **13**, 3237 (2022).

Acknowledgements

Author contributions

J.K. and N.P. conceived the ideas of this study. B.K. performed the first-principles calculations and K.-W.K. carried out the model Hamiltonian calculations. All authors discussed the result and analyzed the data. B.K., D.S., K.-W.K., and J.K. wrote the manuscript together. J.K. supervised the research. B.K. and D.S. contributed equally to this work.

Competing interests

The authors declare no competing interests.

Supplementary Information for

Optoelectronic manifestation of orbital angular momentum driven by chiral hopping in helical Se chains

Bumseop Kim[1,6], Dongbin Shin[2,3,6], Seon Namgung[1], Noejung Park[1], Kyoung-Whan Kim[4*], Jeongwoo Kim[5*]

[1]*Department of Physics, Ulsan National Institute of Science and Technology, Ulsan 44919, Korea*

[2]*Department of Physics and Photon Science, Gwangju Institute of Science and Technology, Gwangju 61005, Korea*

[3]*Max Planck Institute for the Structure and Dynamics of Matter and Center for Free Electron Laser Science, 22761 Hamburg, Germany*

[4]*Center for Spintronics, Korea Institute of Science and Technology, Seoul 02792, Korea*

[5]*Department of Physics, Incheon National University, Incheon 22012, Korea*

[6]These authors contributed equally: Bumseop Kim, Dongbin Shin

*corresponding author e-mail

kwk@kist.re.kr; kjwlou@inu.ac.kr

Supplementary Note 1 | Diagonalisation of the model Hamiltonian for a one-dimensional chiral Se chain.

Here we diagonalise the 9×9 matrix

$$H = \begin{pmatrix} h_{\text{on}} & h_{\text{hop}} & h_{\text{hop}}^{\dagger} \\ h_{\text{hop}}^{\dagger} & h_{\text{on}} & h_{\text{hop}} \\ h_{\text{hop}} & h_{\text{hop}}^{\dagger} & h_{\text{on}} \end{pmatrix}, \tag{S1}$$

in the $|A\rangle, |B\rangle, |C\rangle$ atomic basis. Here h_{on} and h_{hop} are given by the following 3×3 matrices, respectively.

$$h_{\text{on}} = \begin{pmatrix} \epsilon_r & 0 & 0 \\ 0 & \epsilon_t & 0 \\ 0 & 0 & \epsilon_z \end{pmatrix}, h_{\text{hop}} = e^{ik_z a} \begin{pmatrix} t_{rr} & -t_{tr} & -t_{zr} \\ t_{tr} & t_{tt} & t_{zt} \\ t_{zr} & t_{zt} & t_{zz} \end{pmatrix}, \tag{S2}$$

in the $|p_r\rangle, |p_t\rangle, |p_z\rangle$ orbital basis. We first diagonalise the atomic degree of freedom. One can show that equation (S1) is diagonalised by the following eigenstates.

$$|\mu\rangle = \frac{1}{\sqrt{3}} \left(e^{-2\pi i \mu/3} |A\rangle + |B\rangle + e^{2\pi i \mu/3} |C\rangle \right), \tag{S3}$$

where $\mu = -1, 0, 1$. The corresponding eigen-Hamiltonians are given by

$$h_{\text{on}} + 2\text{Re}\left[e^{2\pi i \mu/3} h_{\text{hop}} \right] \tag{S4}$$

which is 3×3 to be diagonalised. Here the real part of a matrix is defined by $\text{Re}[X] = (X + X^{\dagger})/2$. More explicitly, equation (S4) is given by

$$\begin{pmatrix} \epsilon_r + 2t_{rr}\cos\tilde{k}_{z,\mu}a & -2it_{tr}\sin\tilde{k}_{z,\mu}a & -2it_{zr}\sin\tilde{k}_{z,\mu}a \\ 2it_{tr}\sin\tilde{k}_{z,\mu}a & \epsilon_t + 2t_{tt}\cos\tilde{k}_{z,\mu}a & 2t_{zt}\cos\tilde{k}_{z,\mu}a \\ 2it_{zr}\sin\tilde{k}_{z,\mu}a & 2t_{zt}\cos\tilde{k}_{z,\mu}a & \epsilon_z + 2t_{zz}\cos\tilde{k}_{z,\mu}a \end{pmatrix}, \tag{S5}$$

where $\tilde{k}_{z,\mu}a = k_z a + 2\pi\mu/3$. Since $|k_z a| \leq \pi/3$, $\tilde{k}_{z,\mu}$ satisfies $|\tilde{k}_{z,\mu}a| \leq \pi/a$. Now the physical meaning of $\tilde{k}_{z,\mu}$ is clear: a generalised Bloch momentum in a quasi-extended Brillouin zone. Ignoring the helical rotation, the three atoms in the unit cell are located periodically so that the Brillouin zone can be extended to a three times larger space. We call this a quasi-extended Brillouin zone since the helical rotation makes such a direct extension impossible. The cost of the extension is the introduction of off-diagonal hopping terms in equation (S5), which corresponds to a discretised version of the gauge potential.

Since exact diagonalisation of equation (S5) is difficult, we treat $t_{\beta\alpha}$ perturbatively.

Perturbation theory gives the following eigenstates of equation (5).

$$|\widetilde{p_r}\rangle = |p_r\rangle + \frac{2it_{tr}\sin\tilde{k}_{z,\mu}a}{\epsilon_r - \epsilon_t}|p_t\rangle + \frac{2it_{zr}\sin\tilde{k}_{z,\mu}a}{\epsilon_r - \epsilon_z}|p_z\rangle, \qquad (S6)$$

$$|\widetilde{p_t}\rangle = |p_t\rangle - \frac{2it_{tr}\sin\tilde{k}_{z,\mu}a}{\epsilon_t - \epsilon_r}|p_r\rangle + \frac{2t_{zt}\cos\tilde{k}_{z,\mu}a}{\epsilon_t - \epsilon_z}|p_z\rangle, \qquad (S7)$$

$$|\widetilde{p_z}\rangle = |p_z\rangle - \frac{2it_{zr}\sin\tilde{k}_{z,\mu}a}{\epsilon_z - \epsilon_r}|p_r\rangle + \frac{2t_{zt}\cos\tilde{k}_{z,\mu}a}{\epsilon_z - \epsilon_t}|p_t\rangle. \qquad (S8)$$

From the expressions equation (S3) and (S6)-(S8), the eigenstates of the full Hamiltonian [equation (S1)] are then given by

$$|\widetilde{p_r,\mu}\rangle = |\widetilde{p_r}\rangle \otimes |\mu\rangle, \qquad (S9)$$

where $\otimes$ is the direct tensor product of the two spaces.

Supplementary Note 2 | Band characterisation of the analytic eigenstates.

To match the eigenstates [equations (S6)-(S8)] with the results from the first-principles calculations (Supplementary Figure 3), we note that $|\widetilde{p_\alpha}\rangle$ is the perturbed eigenstate due to the hopping elements. Therefore, without hopping, *i.e.*, $\tilde{k}_{z,\mu} = 0$ gives the unperturbed eigenstates. Therefore, the orbital character at the zone center gives the characterisation of each eigenstates. For instance, the top band in Supplementary Fig. 3b is $|\widetilde{p_z}\rangle$. Since $\tilde{k}_{z,\mu}$ is a momentum in a quasi-extended Brillouin zone, there are corresponding three bands in the first Brillouin zone. Therefore, it is natural to conclude that the top three bands correspond to $|\widetilde{p_z,\mu}\rangle$ for three μ values. Similarly, the three valence bands correspond to $|\widetilde{p_t,\mu}\rangle$. Our calculation for a wider energy range (not shown) shows that $|\widetilde{p_r,\mu}\rangle$ are located far below $|\widetilde{p_t,\mu}\rangle$.

Supplementary Note 3 | The relation between orbital angular momentum and injection current in a one-dimensional chiral Se chain.

According to Ref. 48 in main text, the photogalvanic current induced by a circularly-polarised light is given by

$$J = -\frac{4\pi e\tau}{\hbar} \int \frac{dk_z}{2\pi}[\Delta v_z(k_z)]v(k_z)\delta(\Delta\epsilon(k_z) - \hbar\omega), \qquad (S10)$$

where τ is the relaxation time, $v_z(k_z)$ is the group velocity, ω is the frequency of the incident light, Δ means the difference between the initial and final states, and $v(k_z) = \left|P^{RCP}(k_z)\right|^2 - \left|P^{LCP}(k_z)\right|^2$ is the optical absorption efficiency difference for the right and left circular polarised lights. Using $\hbar v_z(k_z) = \partial_{k_z}\epsilon$, equation (S10) is converted to an energy integration.

$$J = -\frac{4\pi e\tau}{\hbar^2} \int \frac{d[\Delta\epsilon(k_z)]}{2\pi}v(k_z)\delta(\Delta\epsilon(k_z) - \hbar\omega) = -\frac{4\pi e\tau}{\hbar^2} \sum_{\Delta\epsilon(k_z)=\hbar\omega} v(k_z). \qquad (S11)$$

When we consider a particular k_z value satisfying $\Delta\epsilon(k_z) = \hbar\omega$, we do not need to keep the summation.

To calculate $P^{RCP/LCP}(k_z)$, it is necessary to calculate the matrix element of the perturbing electric field of the light. In Ref. 48, the system is periodic so that the velocity gauge was used, *i.e.*, $P^{RCP/LCP} = (eA/m_e)\langle v|(p_x \pm ip_y)|c\rangle$, where A is the magnitude of the incident vector potential. However, for our case, the system is confined along the x and y direction so that the position gauge is more preferred, *i.e.*, $P^{RCP/LCP} = eE\langle v|(x \pm iy)|c\rangle$ where E is the magnitude of the incident electric field. Then, one can show that $v = e^2E^2\text{Im}[\langle I|x|F\rangle\langle F|y|I\rangle]$, where I and F are the initial and the final states, respectively. As a result, we obtain

$$J = -\frac{4\pi e\tau}{\hbar^2}e^2E^2\text{Im}[\langle c|x|v\rangle\langle v|y|c\rangle], \qquad (S12)$$

and if there are multiple k_z points satisfying $\Delta\epsilon(k_z) = \hbar\omega$, the contributions should be summed up. Combining equation (S12) and equation (5) gives equation (6) in the main text.

Supplementary Note 4 | Symmetry analysis of the emergence of nonzero orbital angular momentum components in bulk Se.

We consider a general three-dimensional system with time-reversal symmetry and a mirror symmetry with respect to the *zx* plane. First, the time-reversal symmetry implies that all the physical relations should be invariant under the transformation $\mathbf{k} \rightarrow -\mathbf{k}$ and $\mathbf{L} \rightarrow -\mathbf{L}$. In other words,

$$
\begin{aligned}
L_x(k_x, k_y, k_z) &= -L_x(-k_x, -k_y, -k_z), \\
L_y(k_x, k_y, k_z) &= -L_y(-k_x, -k_y, -k_z), \\
L_z(k_x, k_y, k_z) &= -L_z(-k_x, -k_y, -k_z).
\end{aligned}
\tag{S13}
$$

Similarly, the *zx* mirror symmetry implies that all the physical relations should be invariant under the transformation $(k_x, k_y, k_z) \rightarrow (k_x, -k_y, k_z)$ and $(L_x, L_y, L_z) \rightarrow (-L_x, L_y, -L_z)$. In other words,

$$
\begin{aligned}
L_x(k_x, k_y, k_z) &= -L_x(k_x, -k_y, k_z), \\
L_y(k_x, k_y, k_z) &= L_y(k_x, -k_y, k_z), \\
L_z(k_x, k_y, k_z) &= -L_z(k_x, -k_y, k_z).
\end{aligned}
\tag{S14}
$$

Now we consider a more simplified case that the system is confined along the *x* and *y* directions. Then, k_x and k_y become meaningless. By the same argument as equations (S13)-(S14), dropping k_x and k_y, one obtains

$$
\begin{aligned}
L_x(k_z) &= -L_x(k_z), \\
L_y(k_z) &= L_y(k_z), \\
L_z(k_z) &= -L_z(k_z).
\end{aligned}
\tag{S15}
$$

Therefore, $L_x(k_z) = L_z(k_z) = 0$ and only $L_y(k_z)$ can survive, which is depicted in Fig. 4b.
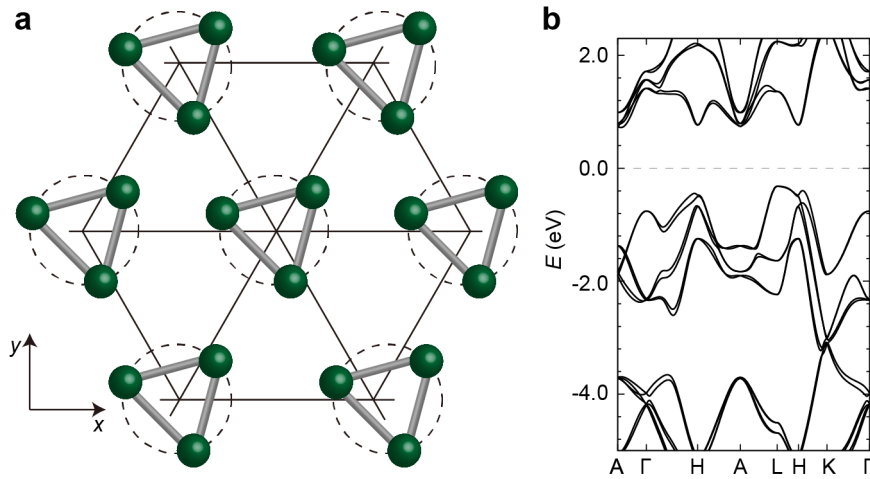
Supplementary Figure 1 | a, b (a) Atomic and **(b)** electronic structure of bulk Se.
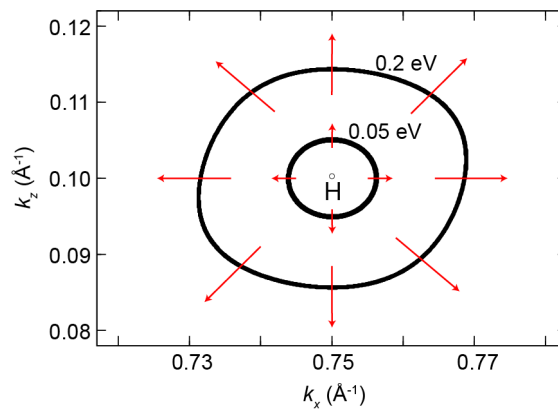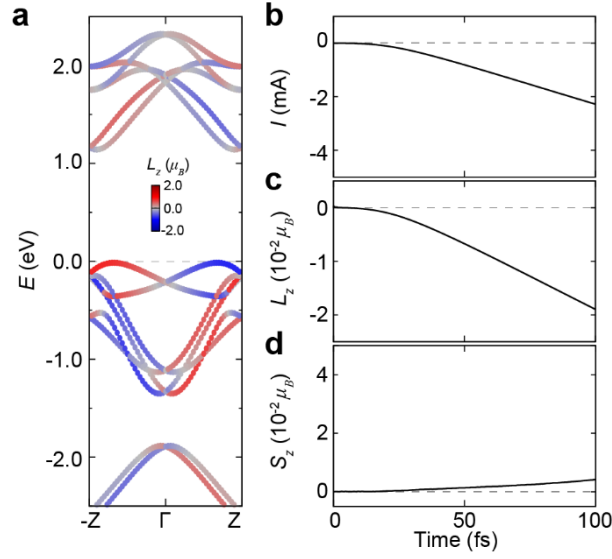

Supplementary Figure 2 | Orbital angular momentum profiles of the conduction band minimum at the H point in bulk Se without the inclusion of SOC. Black contour lines denote energy levels of 0.05 and 0.2 eV, respectively.
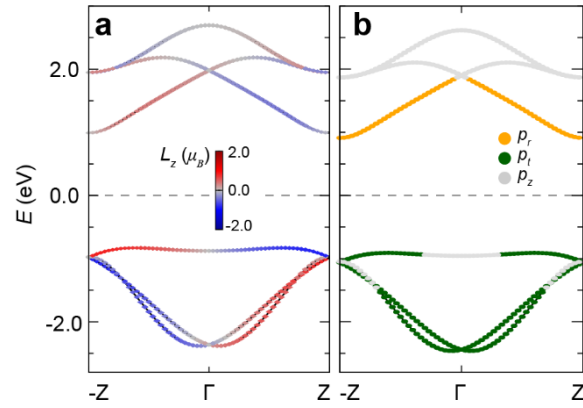
Supplementary Figure 3 | a, b Calculated band structure of a Se chain with (**a**) orbital-angular-momentum resolution (L_z), and (**b**) atomic-orbital resolution using radial (p_r), tangential (p_t), and axial (p_z) p-orbitals as the orbital bases.
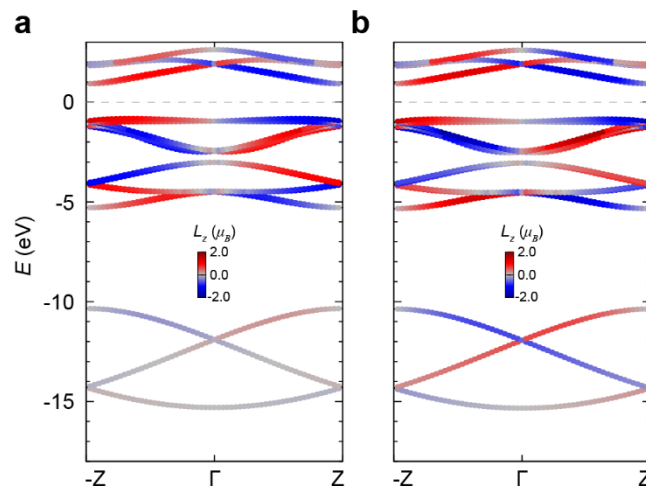
Supplementary Figure 4 | a, b Calculated band structure of a Se chain with orbital-angular-momentum resolution (L_z) using the method of (**a**) atomic orbital decomposition and (**b**) $\mathbf{r} \times \mathbf{p}$ operation.

Supplementary Figure 5 | a Calculated band structure of a Te chain with orbital-angular-momentum resolution (L_z) under hole doping (0.1 e/unit) in the presence of SOC. **b-d** Calculated (**b**) induced current (I), (**c**) total orbital angular momentum (L_z), and (**d**) total spin angular momentum (S_z) induced by a dc field (10^{-3} V/Å) along the Te chain. The quantitative definitions of I, L_z, and S_z are described in the Methods section.
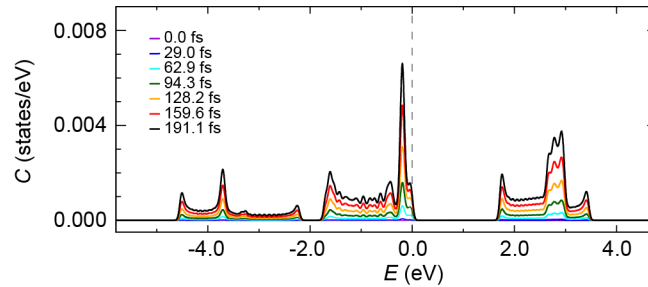
Supplementary Figure 6 | Time evolution of the density of states projected onto the unperturbed electron/hole states in a Se chain under a 0.0001 V/Å field.
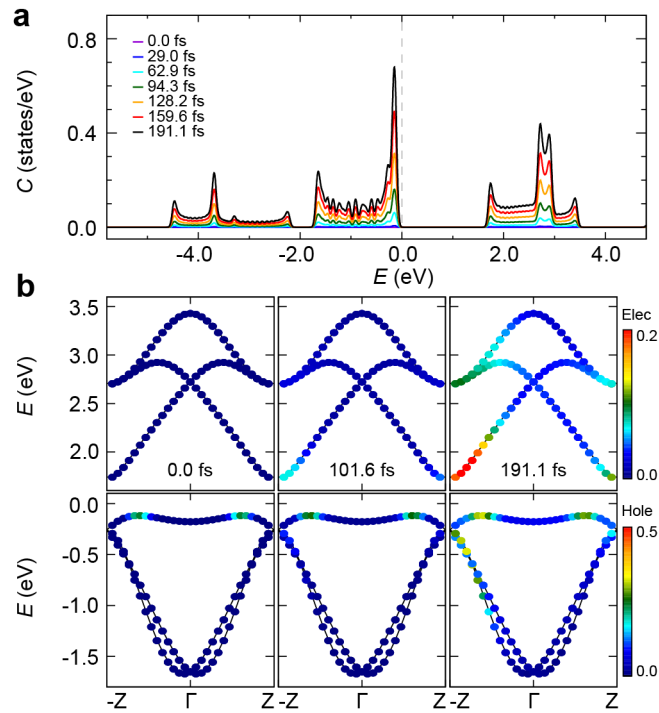
Supplementary Figure 7 | a Time evolution of the density of states projected onto the unperturbed electron/hole states in a Se chain without the inclusion of SOC. **b** Time evolution of the electron/hole weights projected onto the ground-state band structure of the Se chain without the inclusion of SOC.
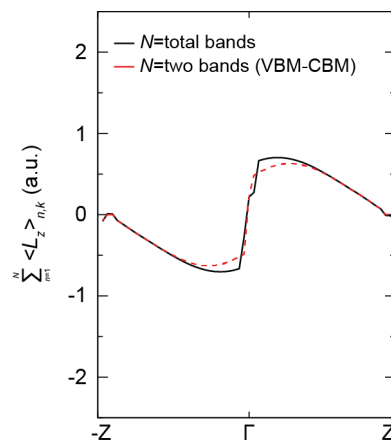

Supplementary Figure 8 | Comparison of total orbital angular momentum and two-band approximated orbital angular momentum.
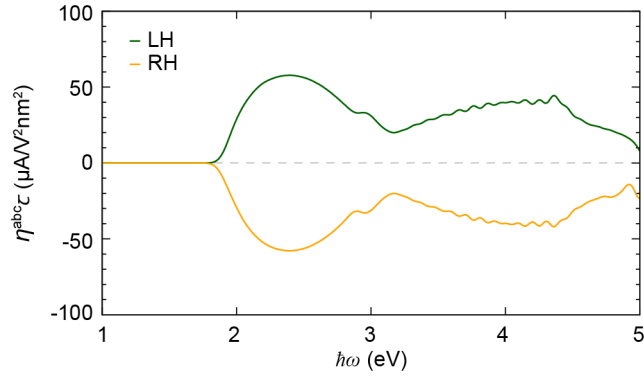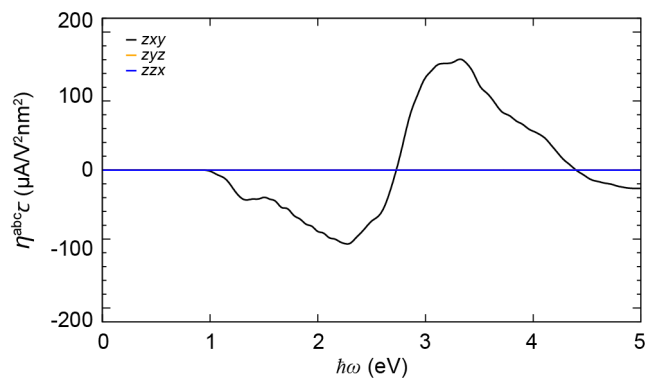
Supplementary Figure 9 | Handedness dependence of calculated circular photogalvanic current (injection current) spectrum of a Se chain as a function of the frequency.
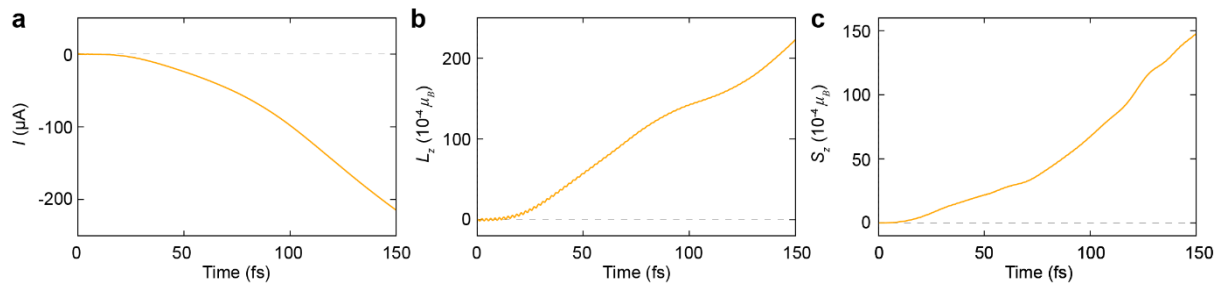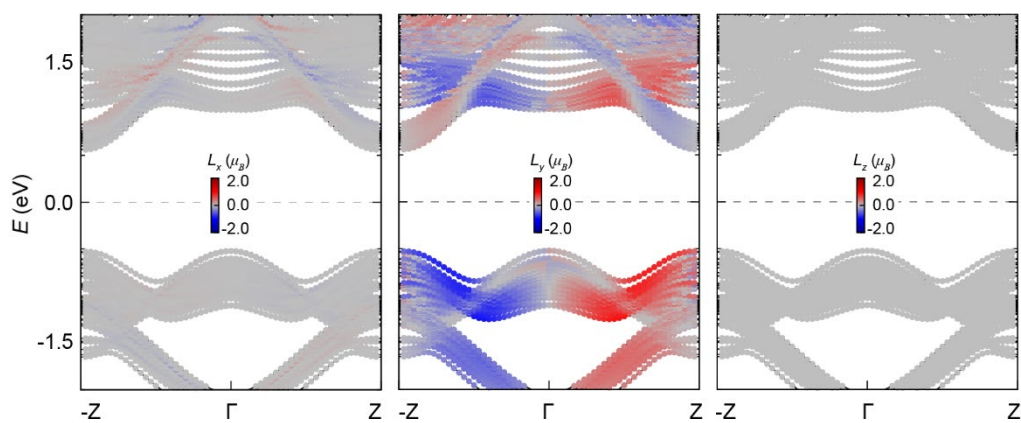

Supplementary Figure 10 | a-c Calculated (**a**) induced current (I), (**b**) total orbital angular momentum (L_z), and (**c**) total spin angular momentum (S_z) induced by a circularly polarised light with intensity of 0.51 V/Å and frequency of $\hbar\omega$=2.02 eV as a function of time.
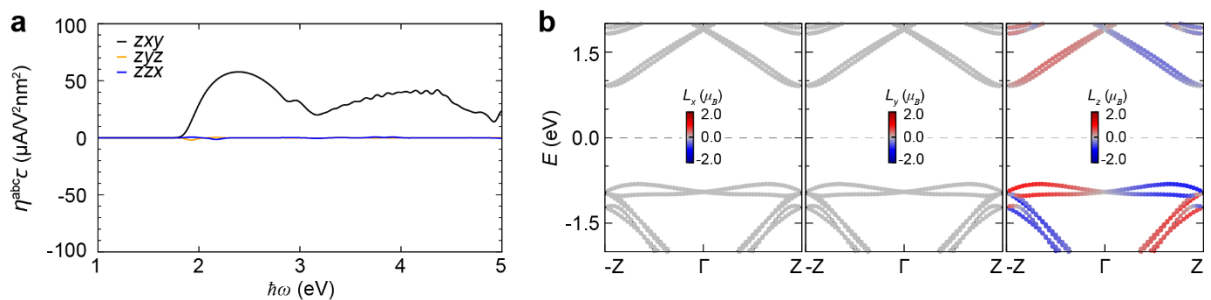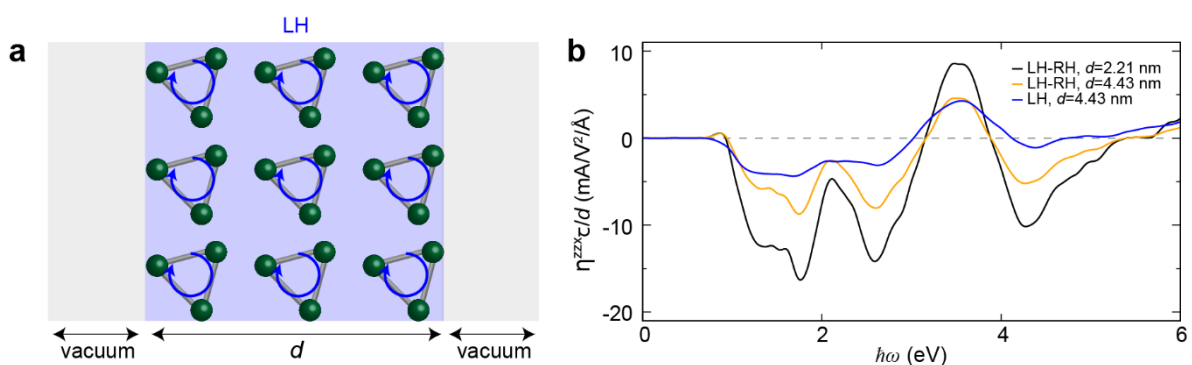

Supplementary Figure 11 | a Calculated circular photogalvanic current (injection current) spectrum of a Se chain as a function of the frequency for various circularly polarised lights. **b** Calculated band structure of the Se chain with orbital-angular-momentum resolution (L_x, L_y, and L_z).

Supplementary Figure 12 | Calculated circular photogalvanic current (injection current) spectrum of bulk Se as a function of the frequency.

Supplementary Figure 13 | Calculated band structure of the domain boundary between LH and RH domains with orbital-angular-momentum resolution (L_x, L_y, and L_z).

Supplementary Figure 14 | a Schematic drawing of a slab structure for left-handed (LH) or right-handed (RH) chains exposed to vacuum. **b** Calculated injection current spectrum per unit length for the LH slab and the LH-RH domain structures with respect to domain length (*d*).